The Astrophysical Journal Supplement Series, 260:47 (14pp), 2022 June https://doi.org/10.3847/1538-4365/ac666b

Long-term Optical Monitoring of the TeV BL Lacertae Object 1ES 2344+514

J. T. Cai[1,2,3,8], S. O. Kurtanidze[4,5,8], Y. Liu[1,2,3], O. M. Kurtanidze[4,5,6], M. G. Nikolashvili[4,5], H. B. Xiao[7], and J. H. Fan[1,2,3]
[1] Center for Astrophysics, Guangzhou University, Guangzhou 510006, People's Republic of China; fjh@gzhu.edu.cn
[2] Astronomy Science and Technology Research Laboratory of Department of Education of Guangdong Province, Guangzhou 510006, People's Republic of China
[3] Key Laboratory for Astronomical Observation and Technology of Guangzhou, Guangzhou 510006, People's Republic of China
[4] Abastumani Observatory, Mount Kanobili, 0301 Abastumani, Georgia
[5] Landessternwarte, Zentrum für Astronomie der Universität Heidelberg, Königstuhl 12, D-69117 Heidelberg, Germany
[6] Engelhardt Astronomical Observatory, Kazan Federal University, Tatarstan, Russia
[7] Shanghai Key Lab for Astrophysics, Shanghai Normal University, Shanghai, 200234, People's Republic of China
Received 2021 December 28; revised 2022 March 17; accepted 2022 April 5; published 2022 June 23

Abstract

Variability is one of the main observational characteristics of blazars. Studying variability is an efficient method to reveal the nature of active galactic nuclei. In the present work, we report optical *R*-band photometry observations of a TeV blazar, 1ES 2344 + 514, carried out with a 70 cm telescope in the period of 1998 July–2017 November at Abastumani Observatory, Georgia. Based on the optical *R*-band observations, the optical variation behaviors on both short timescales and long timescales are investigated. Three methods (Jurkevich, discrete correlation function, and power spectrum analysis) are used to investigate periodicity in the light curve. In addition, combined with multiwavelength data, the jet physical properties are discussed. The following conclusions are drawn: (1) A variability of $\Delta R = 0.155$ mag ($15.356 - 15.201$ mag) over a timescale of $\Delta T = 12.99$ minutes is detected during our 628 days of monitoring. (2) According to the Kelvin–Helmholtz thermal instability, if the magnetic field intensity (B) for the source is greater than a critical value (B_c), it will reduce the incidence of intraday variations in the light curves. (3) The physical parameters of the dissipation region are obtained by fitting the spectral energy distribution with a one-zone synchrotron self-Compton model for the average and flare states. (4) The three methods show that there are periods of $P = 2.72 \pm 0.47$ yr, $P = 1.61 \pm 0.18$ yr, $P = 1.31 \pm 0.17$ yr, and $P = 1.05 \pm 0.07$ yr. When a binary black hole system is adopted with a period of $P = 2.72 \pm 0.41$ yr, we obtain the orbital parameters for the binary black hole system as follows: $M = 8.08 \times 10^9 M_\odot$, the sum of the semiaxes is $r = 7.18 \times 10^{16}$ cm, and the lifetime of the binary black hole is $\tau_{\rm merge} = 6.24 \times 10^2$ yr.

Unified Astronomy Thesaurus concepts: Active galactic nuclei (16); CCD photometry (208); Quasars (1319)

Supporting material: machine-readable table

1. Introduction

Blazars display extreme observational properties, such as rapid and high-amplitude variability, high and variable polarization, a nonthermally dominated continuum, highly energetic γ-ray emissions, and superluminal motions (Blandford & Rees 1978; Angel & Stockman 1980; Urry & Padovani 1995; Hartman et al. 2001; Ackermann et al. 2015; Fan et al. 2016, 2017a, 2017b, 2018, 2021; Xiao et al. 2019). In the unified model of active galactic nuclei (AGNs), blazar jets point toward us within a very narrow angle of 10° (Blandford & Koenigl 1979; Urry & Padovani 1995). Blazars are a subclass of AGNs, and they have two further subclasses, BL Lacertae objects and flat-spectrum radio quasars, based on their optical spectra. The former one characterizes a spectrum with no or weak emission lines (rest-frame equivalent width EW < 5 Å), while the latter one shows strong emission line features of EW ⩾ 5 Å (Urry & Padovani 1995; Scarpa & Falomo 1997). The spectral energy distributions (SEDs) of blazars usually show a typical bimodal behavior. The low-energy bump is derived from relativistic electron synchrotron radiation in the jet. The origin of the high-energy bump is controversial. There are two models: the leptonic model and the hadronic model. The leptonic model mainly involves inverse Compton (IC) scattering of relativistic electrons from the jets, in which soft photons may originate from their own synchrotron radiation or from the external region (the accretion disk, broad-line region, torus, or cosmic microwave background radiation) (Maraschi et al. 1992; Dermer & Schlickeiser 1993; Sikora et al. 1994; Bloom & Marscher 1996; Błażejowski et al. 2000; Fan et al. 2006). The hadronic model holds that protons and electrons in the jet are accelerated to extremely relativistic levels. Synchrotron radiation of extremely relativistic high-energy protons or interaction of high-energy protons with low-energy photons or gas clouds produces high-energy γ-ray radiation (Aharonian 2000, 2002). In some cases, if the host galaxy contribution is strong, it will be present in the infrared to optical bands of the low-energy bump. The host galaxy will have an influence on the SED, color index, and spectral index. Therefore, it is necessary to make corrections for the host galaxy (see, e.g., Nilsson et al. 2007).

The synchrotron peak frequency ($\log \nu_s$) is used to classify blazars (Abdo et al. 2010; Nolan et al. 2012; see also Padovani & Giommi 1996; Nieppola et al. 2006). Following Abdo et al. (2010), Fan et al. (2016) suggested that blazars are classified as low-synchrotron-peaked blazars if $\log \nu_p \leqslant 14.0$ Hz, as intermediate-synchrotron-peaked blazars if $14.0 < \log \nu_p \leqslant 15.3$ Hz, and as high-synchrotron-peaked blazars if $\log \nu_p > 15.3$ Hz based on an SED fitting study of 1392 Fermi blazars.

[8] J. T. Cai and S. O. Kurtanidze contributed equally to this work.

Using variability is one of the important methods to study the blazar emission mechanism. From the variability timescale, variability is classified as intraday variability with timescales within 1 day, as short-term variability with timescales of a few days to months, and as long-term variability with timescales of years (Fan 2005). For less than 1 day variability, it is called microvariability if a source shows a brightness variation in a very short time (Miller et al. 1989), or intraday variations (IDVs) (Wagner & Witzel 1995), or intranight variations (Sagar et al. 1996). In general, an IDV is not periodic. Several theoretical models have been proposed to explain this phenomenon—for instance, the relativistic jet and the thin disk instability model. Long-term variations are sometimes periodic (Jurkevich 1971; Sillanpaa et al. 1988; Fan et al. 1998, 2002, 2007, 2018; Ciaramella et al. 2004; Qian & Tao 2004; Ciprini et al. 2007; Valtonen et al. 2008; Rani et al. 2010; Wiita 2011; Gaur et al. 2012; Gupta 2014; Li et al. 2015). Periodicity has been demonstrated for some well-known BL Lac objects (e.g., OJ 287, BL Lacertae, 0716+714, 3C 66A, Mrk 421, AO 0235+164, ON 231, and Mrk 501) by many authors (Sillanpaa et al. 1988; Liu et al. 1996; Fan et al. 1998; Zhang et al. 1998; Fan & Lin 2000; Fan et al. 2007, 2017a, 2018; Raiteri et al. 2012). In general, the optical periodic behavior can be explained by the binary black hole model, the thermal instability model, and the perturbation model (Meyer & Meyer-Hofmeister 1984; Sillanpaa et al. 1988; Romero 1995; Rieger 2004; Xie et al. 2004; Wu et al. 2005; Fan et al. 2021).

1ES 2344 + 514 ($\alpha_{2000} = 23^{h}47^{m}0\overset{s}{.}48; \delta_{2000} = +51°42'17\overset{''}{.}9$), $z = 0.044$, is a BL Lac object with TeV γ-ray emission (>350 GeV) as observed by the Wipple Observatory telescope (Catanese et al. 1998). Giommi et al. (2000) reported rapid variation in the X-ray band over a timescale of 5000 s. Grube (2008) suggested that Major Atmospheric Gamma-ray Imaging Cherenkov (MAGIC) observed high-energy radiation from 1ES 2344 + 514, which showed flux variation over the 300 GeV range. At the very high energy (VHE) γ-ray band ($0.1 < E < 300$ GeV), 1ES 2344 + 514 is associated with the object 4FGL J2347.0 + 5141 in the latest catalog of Fermi/LAT (Abdollahi et al. 2020). Acciari et al. (2011) made the first multiband observations for 1ES 2344 + 514 at the UV, X-ray, and VHE bands for several months.

Similar to the multiband observations that have been investigated, the variability of 1ES 2344 + 514 has been studied in the literature. Miller et al. (1999) observed 1ES 2344 + 514 with a *BVR* filter and found a positive about 0.08 mag microvariability on 1996 September 20. Later on, Dai et al. (2001) reported their optical observations and found a 0.14 mag IDV in the *V* band within 26 minutes. In order to study long-term variations and IDVs, optical *R*-band observations of two TeV BL Lac sources 1ES 1959 + 650 and 1ES 2344 + 514 have been carried out with the 70 cm telescope in Abastumani Observatory, Georgia (Kurtanidze & Nikolashvili 2002; Kurtanidze et al. 2003, 2004, 2005). These sources were observed for 72 nights and 39 nights, respectively. IDVs did not surpass 0.01 mag for these two targets, and no evidence of IDV was found for 1ES 2344 + 514 within a few hours or less. Subsequently, Xie et al. (2002) monitored the source at the optical *VR* bands and did not detect IDVs either. Fan et al. (2004) observed the source, but no IDV was observed in the *R* band. Ma et al. (2010) claimed that the brightness of the optical *R* band varied by 0.69 ± 0.16 mag over a timescale of 4738 s, which is seemingly coincidental to the rapid variation found in the X-ray at 5000 s (Giommi et al. 2000). 1ES 2344 + 514 was observed for 19 nights in 2009–2010 (Gaur et al. 2012), and no significant IDV was found although long-term variation existed. Recently, Pandey et al. (2020) reported observations of 1ES 2344 + 514 with two telescopes (1.3 m Devasthal and 1.4 m Sampuranand) but they did not observe any obvious IDVs.

In the present work, we report 19.3 yr of observations from the source 1ES 2344 + 514 at Abastumani Observatory in Georgia with a 70 cm telescope. Based on these data, the IDV will be investigated by three methods. This work is arranged as follows. In Section 2, we will introduce the observations and data processing. In Sections 3 and 4, we describe the analysis of the data, present a discussion, and offer conclusions.

2. Observation and Data Processing

2.1. Photometry Process

The systematic blazar optical monitoring program in Abastumani was started in 1997 February with a dedicated 70 cm meniscus telescope and SBIG ST-6 CCD camera attached to a Newtonian focus (Kurtanidze et al. 1999, 2001b; Kurtanidze & Nikolashvili 2001a). The targets, over 50 sources, were selected from the Catalogue of Quasars and AGNs (Veron-Cetty & Veron 1993) and the Einstein Slew Survey sample of BL Lac objects (Perlman et al. 1996). About 80% of the sources selected from the Einstein Slew Survey were later discovered as TeV-emitting extragalactic sources.

Abastumani Observatory is located on top of Mount Kanobili in the southwestern part of Georgia at an altitude of 1700 m above sea level with latitude and longitude of $41\overset{\circ}{.}8051$ and $42\overset{\circ}{.}8254$, respectively. The weather and seeing conditions there are good: about half of the year has clear weather, in which a third of the seeing is below 1″.

The mean sky brightness in *BVRI* is 22.0, 21.2, 20.6, and 19.8 mag, respectively. All observations of 1ES 2344 + 514 were conducted on a 70 cm meniscus telescope ($f/3$) using front-illuminated CCD cameras SBIG ST-6 (1998–2006, 375×242, 23×27 μm pixels, quantum efficiencies of 0.30 at 400 nm and 0.6 at 680 nm, field of view (FOV) = 14.9×10.7 arcmin^2) and Apogee Ap6E (2006–2018, 1024×1024, 24 μm pixels, quantum efficiencies of 0.4 at 400 nm and 0.67 at 680 nm) attached to the prime focus of the meniscus telescope. In the case of ST-6 we used the full frame, while for Ap6E we used 350 pixels (FOV = 15×15 arcmin^2) located in the center part of the chip, and the entire FOV was 40×40 arcmin^2.

2.2. Data Reductions

The observations were conducted using the *R*-band filter with exposure time ranging from 60 to 300 s. Image processing (bias correction, flat-fielding, cosmic-ray removal, etc.) and differential photometry of the images in an aperture of 10″ were performed using the Daophot II program (Stetson 1987). Final calibrations of the magnitudes were done using comparison stars in the field (Fan et al. 2004).

First, we chose the comparison stars. For all the comparison stars, if m_i and m_j were the magnitudes of the comparison stars S_i and S_j, the corresponding magnitude difference was $\Delta m_{ij} = m_i - m_j$, and the standard deviation of any two compared stars was $\sigma_{m_{ij}}$. Then, we chose the two standard stars with the least deviation as comparison stars S_1 and S_2. Second, the magnitude of the target star was obtained by

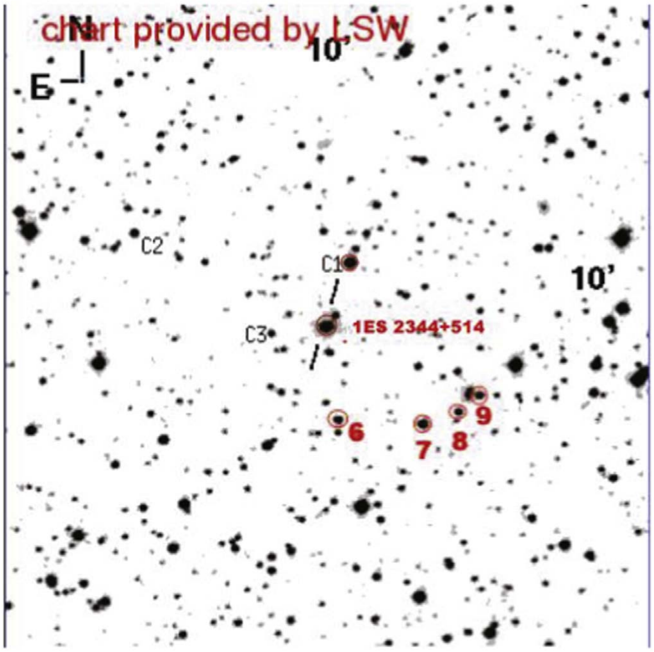

Figure 1. The source of 1ES 2344 + 514 in the image from LSW.

comparing S_1 and S_2. First, $O - S_1$ and $O - S_2$ were calculated, and then the sizes m_{S_1} and m_{S_2} were obtained; finally, we derived the average value $m_O = \frac{1}{2}(m_{S_1} + m_{S_2})$ as the target magnitude. The standard deviation of the two comparison stars ($S_1 - S_2$) was used as the uncertainty of the target.

For 1ES 2344 + 514, we obtained the magnitude differences between the comparison star C1 at LSW[9] and stars 6, 7, 8, and 9 by photometry, which are marked in Figure 1, and also listed in Table 1. From our calculations, comparison stars 6 and 7 were selected as the comparison stars in our photometry determinations.

We obtained 3136 pairs of observations in an observation period of 19.33 yr. The daily averaged magnitudes are listed in Table 2. The first column of Table 2 is the time (JD 2,451,021+), the second column is the magnitude, and the third column is the uncertainty. According to $f_R = 3.08 \times 10^{6-0.4m_R}$ mJy (Mead et al. 1990), the corresponding minimum flux is 4.33 ± 0.11 mJy, and the maximum flux is 6.15 ± 0.05 mJy with an average flux of 5.20 ± 0.05 mJy.

Optical emissions include the contribution of the host galaxy, which should be subtracted when we investigate variability properties. Nilsson et al. (1999) pointed out that the contribution of the host galaxy depends on the aperture radius during photometry, and they obtained an R magnitude, $R_{\rm host} = 14.90$ mag, of the host galaxy using a 10″ aperture for 1ES 2344 + 514. $R_{\rm host} = 14.90$ mag corresponds to a flux density of $f_{\rm host} = 3.37$ mJy. In our observations in Abastumani Observatory, we used a 10″ aperture. Therefore, in our analysis, we first derived the Galactic extinction for the obtained magnitude using $A_R = 0.458$ (Schlafly & Finkbeiner 2011), and then we translated the R magnitude into flux density using $f_R = 3.08 \times 10^{6-0.4m_R}$ mJy (Mead et al. 1990); afterward we subtracted the contribution of the host galaxy and obtained the source flux density $f_R^S = f_R - f_{\rm host}$. Finally, we used the flux or the magnitude translated from f_R^S for our analysis throughout the work. The corresponding light curve is shown in Figure 2.

[9] https://www.lsw.uni-heidelberg.de/projects/extragalactic/charts/2344+514.html

Table 1
Comparison Stars for 1ES 2344 + 514

Star	Magnitude	C1 – X
C1	12.25 ± 0.04	…
6	14.28 ± 0.01	−2.02
7	13.43 ± 0.01	−1.19
8	14.71 ± 0.01	−2.46
9	14.60 ± 0.01	−2.35

Notes. Column (1): Check star (C1) and comparison stars (6, 7, 8, and 9, marked "X" in the table). Column (2): Magnitude and uncertainty. Column (3): Magnitude difference between C1 and comparison star.

Table 2
Observational Data for 1ES 2344 + 514

JD +2,451,021	m_R (mag)	σ_{mR} (mag)
(1)	(2)	(3)
0.42997	14.3794	0.0093
19.38895	14.4283	0.0113
35.47073	14.4296	0.0076
47.48564	14.4537	0.0059
50.44220	14.4244	0.0197
52.44141	14.4502	0.0028
55.43282	14.3713	0.0057
63.40993	14.4160	0.0008

Note. This table is available in its entirety in machine-readable and Virtual Observatory form in the online journal.

(This table is available in its entirety in machine-readable form.)

2.3. Test Methods for Variation

Variations were tested using a C-test (Romero et al. 1999; Cellone et al. 2000) and an F-test (de Diego 2010). If a variation occurred, then the variation amplitude Amp and the corresponding time interval were obtained; the time interval was taken as the timescale ΔT.

C-test: In this test, a parameter C was introduced to judge whether the source had a variation or not. The parameter C was defined as

$$C_A = \frac{\sigma_{\rm (BL-StarA)}}{\sigma_{\rm (StarA-StarB)}} \left(\text{or } C_B = \frac{\sigma_{\rm (BL-StarB)}}{\sigma_{\rm (StarA-StarB)}} \right), \tag{1}$$

where $\sigma_{\rm (BL-StarA)}$, $\sigma_{\rm (BL-StarB)}$, and $\sigma_{\rm (StarA-StarB)}$ denote the standard deviations of the magnitude difference between the blazar and comparison star A, that between the blazar and comparison star B, and that between comparison stars A and B, respectively. The corresponding uncertainties were

$$\sigma = \sqrt{\frac{\sum(m_i - \overline{m})^2}{N-1}}. \tag{2}$$

If $C = \frac{C_A + C_B}{2} > 2.576$, then the source had undergone variability during the observation period (Romero et al. 2000).

F-test: An F-test is a distribution statistical method for detecting variability proposed by de Diego (2010) that uses

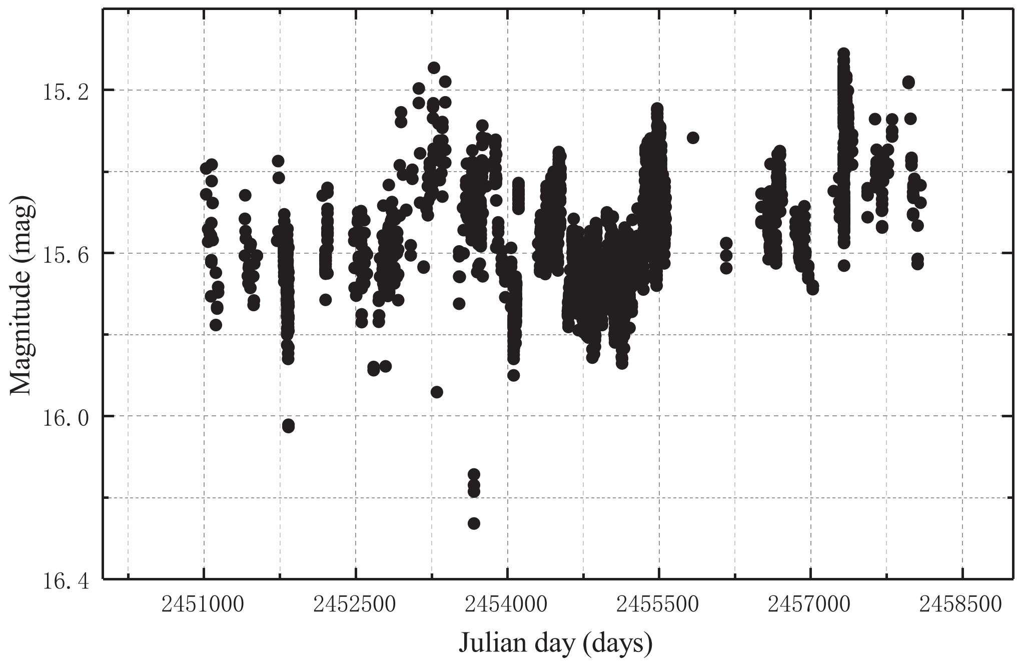

Figure 2. The optical R-band light curve. The data from 1ES 2344 + 514 shown here were corrected for the host galaxy contribution and Galactic reddening.

different comparison stars as reference samples. F-test statistics are defined as

$$F_1 = \frac{S^2_{\mathrm{BL-StarA}}}{S^2_{\mathrm{StarA-StarB}}},\ F_2 = \frac{S^2_{\mathrm{BL-StarB}}}{S^2_{\mathrm{StarA-StarB}}}, \tag{3}$$

where $S^2_{\mathrm{BL-StarA}}$, $S^2_{\mathrm{BL-StarB}}$, and $S^2_{\mathrm{StarA-StarB}}$ represent the variance of the instrument magnitude difference between the blazar and comparison star A, that between the blazar and comparison star B, and that between comparison stars A and B, respectively. The statistics $F_{1,2}$ calculated by the F-test are compared with a critical value $F^{\alpha}_{\nu_{\mathrm{BL}},\nu_c}$, where $\nu_{\mathrm{BL}} = \nu_c$, the pair number of observations minus one, denotes the degrees of freedom of the comparison star, and α denotes the significance level of the test. For the significance level parameters of the F-test in this paper, α was selected as 0.99 and 0.999. When F_1 and F_2 were both greater than the critical value of the significance level of 0.999, they judged the changes in brightness. When they were both greater than the critical value of the significance level of 0.99, and less than that of 0.999, they might have had variation (de Diego 2010; see also Gaur et al. 2012; Xiong et al. 2017; Fan et al. 2021).

The magnitude of variation can be calculated as (Heidt & Wagner 1996)

$$\mathrm{Amp} = \sqrt{(m_{\max} - m_{\min})^2 - 2\overline{\sigma}^2}\,(\%), \tag{4}$$

where $m_{\max}$ and $m_{\min}$ represent the maximum and minimum magnitude during the observation period, and $\overline{\sigma}$ represents the average value of the corresponding uncertainties.

3. Results

3.1. Variation

We observed the source 1ES 2344 + 514 for a total of 628 nights in the optical R band, and performed variation tests on each night. It was considered that a variation was true when the brightness variation met the following requirements: (1) the amplitude of variation Amp is not lower than 3σ (Fan et al. 2009a, 2009b, 2014), (2) the variational parameter $C \geqslant 2.576$ (Romero et al. 2000), and (3) the variation meets the F-test criterion (de Diego 2010).

We performed intraday variability tests for each observational night during the period of 1998 October to 2017 February. We used the above three detection methods to carefully check whether there was an IDV. During the whole observation period, a maximum variation $\Delta R = 1.154$ mag (from $R = 15.110$ mag to $R = 16.263$ mag) was found. From Figure 3, we can see that 1ES 2344 + 514 exhibited an IDV on JD 2,457,367, its brightness increased from $R = 15.356$ mag to $R = 15.201$ mag within 12.99 minutes, and the corresponding variability amplitude and variability parameters were $A = 15.45\%$, $C_1 = 4.15$, $C_2 = 4.52$, $F_1 = 28.64$, and $F_2 = 32.96$. Our observations and the corresponding values of IDVs are clearly shown in Table 3. Please refer to the notes for details.

In addition, we found 16 nights of results that gave F-test values F_1, $F_2 < F^c_{99}$, and corresponding C-test values C_1, $C_2 > 2.576$. These 16 nights were on JD 2,451,068, JD 2,452,584, JD 2,452,854, JD 2,453,302, JD 2,453,565, JD 2,453,668, JD 2,453,752, JD 2,453,890, JD 2,454,303, JD 2,454,465, JD 2,454,618, JD 2,455,497, JD 2,456,664, JD 2,456,886, JD 2,457,327, and JD 2,458,054. On JD 2,457,327, the brightness increased from $R = 15.631$ mag to $R = 15.201$ mag, indicating a variability of $A = 20.16\%$ over 1.03 minutes. The C-test and F-test values were $C_1 = 8.21$, $C_2 = 7.21$, $F_1 = 6.28$, and $F_2 = 5.81$. However, there were only two pairs of observations, and the critical values were $F^c_{99} = 4063$ and $F^c_{99.9} = 10{,}000$. If this IDV is true, it is the fastest brightness variation for the source.

We report the results of short-timescale variation (STV) studies of the source. We also used three variational parameters to test the results of STVs—Amp, C-test, and F-test—and the results are shown in Table 4 and Figure 4.

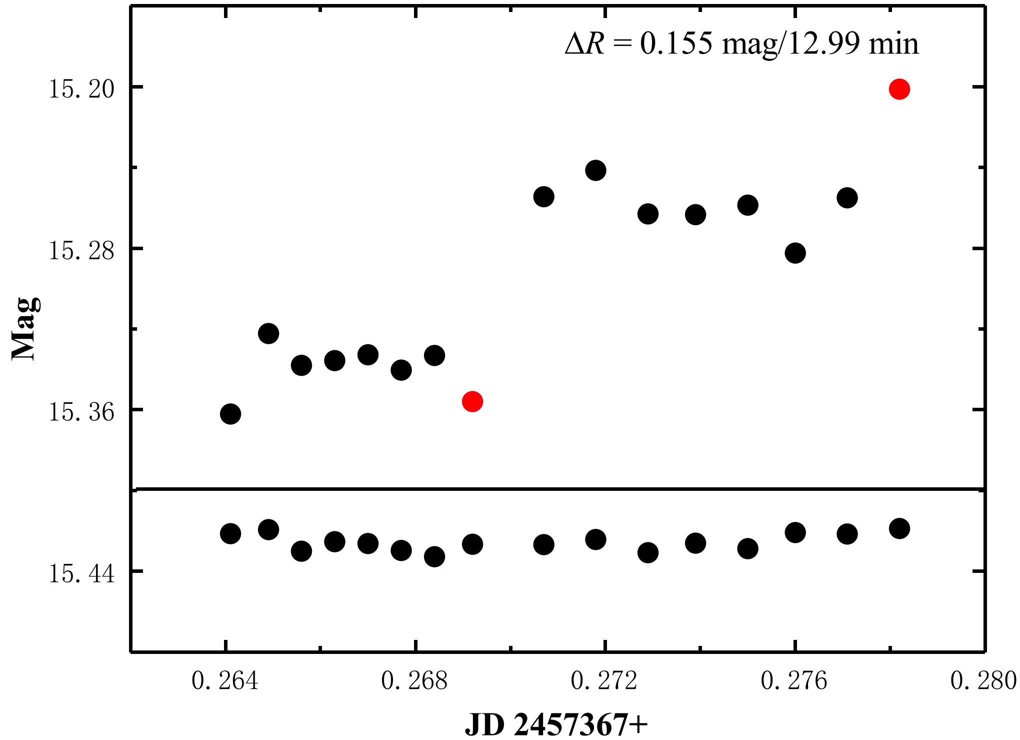

Figure 3. IDV on JD 2,457,367. The upper subpanel is for the light curve, while the lower subpanel is for the differential light curve of the two comparison stars plus a constant.

Table 3
The Intraday Variability Results of 1ES 2344 + 514

JD 2,450,000+ (1)	m_1 (2)	m_2 (3)	σ (4)	Num (5)	C_1 (6)	C_2 (7)	F_1 (8)	F_2 (9)	F^c_{99} (10)	$F^c_{99.9}$ (11)	A (%) (12)	ΔT (min) (13)	Var (14)
1068.4814	15.7061	15.5571	0.0042	2	5.50	6.50	30.25	42.25	4063	20,000	14.89	12.20	P
2584.2755	15.6744	15.5191	0.0074	2	4.10	3.10	16.81	9.61	4063	20,000	15.50	7.99	P
2854.3343	15.5985	15.5598	0.0019	2	4.05	3.05	16.42	9.32	4063	20,000	3.86	5.70	P
3302.5019	15.9413	15.3681	0.0010	2	90.71	91.71	8229.08	8411.51	4063	20,000	57.31	6.72	P
3565.4982	15.6007	15.5436	0.0006	2	17.17	16.17	294.69	261.36	4063	20,000	5.71	7.78	P
3668.3190	16.2634	15.4063	0.0207	4	5.31	6.12	14.30	21.44	29.20	140.00	85.66	25.75	P
3752.2407	15.3994	15.2865	0.0037	3	5.61	5.37	33.57	30.81	99.00	999.00	11.28	9.26	P
3890.5116	15.5861	15.5474	0.0055	3	6.24	6.35	20.95	23.72	99.00	999.00	22.85	11.26	P
4303.4669	15.6081	15.5762	0.0015	2	4.31	3.31	18.58	10.96	4063	20,000	3.18	3.02	P
4465.2588	15.5659	15.5009	0.0032	4	3.26	3.11	9.83	7.72	29.20	140.00	6.48	12.12	P
4618.5046	15.5046	15.5109	0.0008	3	5.61	6.27	31.48	39.37	99.00	999.00	3.32	9.09	P
5497.3759	15.3388	15.2997	0.0010	2	8.84	7.84	15.81	10.96	4063	20,000	3.91	6.06	P
6664.2477	15.4818	15.4129	0.0012	2	10.88	9.88	12.66	14.77	4063	20,000	6.88	3.02	P
6886.5089	15.6128	15.5267	0.0022	3	5.94	6.25	35.22	39.06	99.00	999.00	8.60	6.06	P
7327.4498	15.6307	15.4290	0.0047	2	8.21	7.21	6.28	5.81	4063	20,000	20.16	1.04	P
7367.2641	15.3559	15.2013	0.0041	9	4.15	4.52	28.64	32.96	6.30	12.00	15.45	12.99	Y
8054.5058	15.6265	15.5326	0.0043	3	3.85	2.93	8.64	99.00	99.00	999.00	9.37	9.10	P

Notes. Column (1): Observing time (JD). Column (2): Magnitude at the variability occurrence point (m_1). Column (3): Magnitude at the variability ending point (m_2). Column (4): Uncertainty of the corresponding night (σ). Column (5): Pairs of observations (N). Column (6): Variability index (C_1) from the difference in magnitude between target and comparison star ($O - S_1$). Column (7): Variability index (C_2) from the difference in magnitude between target and comparison star ($O - S_2$). Column (8): F-test value (F_1) from target and comparison star ($O - S_1$). Column (9): F-test value (F_2) from target and comparison star ($O - S_2$). Column (10): Critical value for the corresponding N at 99% level. Column (11): Critical value for the corresponding N at 99.9% level. Column (12): Variability amplitude (A%). Column (13): Corresponding timescale in units of minutes. Column (14): Variability (Y: has a variation; P: has a possible variation).

From Figure 4(a), it can be obtained that the faintest moment of $R = 15.536$ mag is JD 2,454,520.18, and the brightest moment is JD 2,451,523.17, corresponding to $\Delta R = 0.174$ mag over 2.99 days, or to a variation amplitude of Amp = 17.36%.

At JD 2,454,499.19, the brightness increased from $R = 15.642$ mag to $R = 15.351$ mag, the amplitude $\Delta R = 0.291$ mag, and the timescale of variation was 8.03 days. The corresponding light curve is shown in Figure 4(b).

The brightness increased from $R = 15.680$ mag at JD 2,455,473.36 to $R = 15.244$ mag at JD 2,455,480.40, the amplitude was $\Delta R = 0.436$ mag, and the corresponding timescale was 7.01 days, as shown in Figure 4(c).

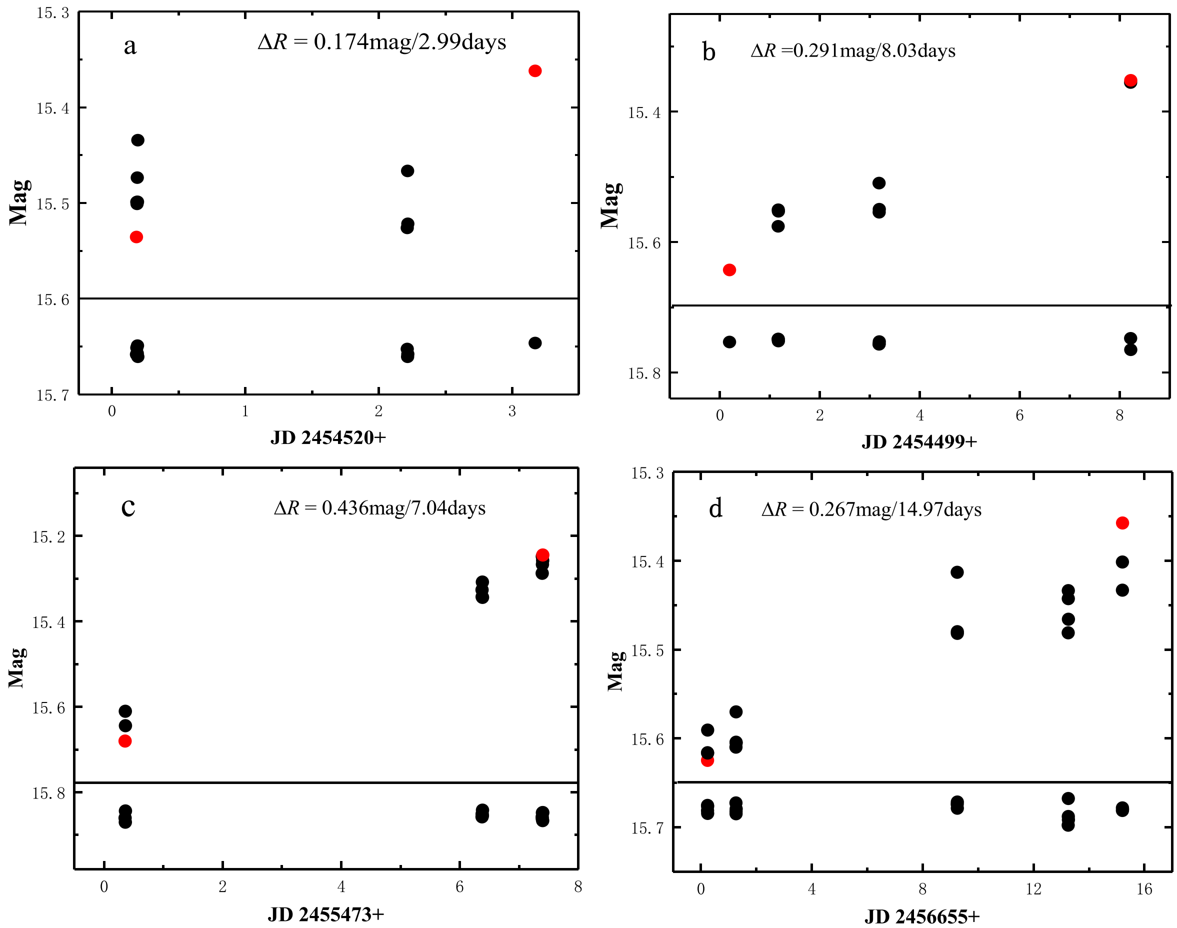

Figure 4. STVs during our monitoring period. In each individual panel, there are two subpanels. The upper subpanel is for the light curve, while the lower subpanel is for the differential light curve of the two comparison stars plus a constant.

Table 4
The STV Results of 1ES 2344 + 514

JD 2,450,000+ (1)	m_1 (2)	m_2 (3)	σ (4)	Num (5)	C_1 (6)	C_2 (7)	F_1 (8)	F_2 (9)	F^c_{99} (10)	$F^c_{99.9}$ (11)	A (%) (12)	ΔT (days) (13)	Var (14)
4060.4975–4110.3189	15.9002	15.4331	0.0104	92	2.66	2.70	7.07	7.30	1.63	1.91	46.69	49.82	Y
4324.5170–4110.3273	15.6455	15.4278	0.0048	12	5.62	6.08	31.57	36.93	4.43	7.70	21.76	214.19	Y
4415.3412–4435.3901	15.6336	15.4139	0.0064	8	3.56	4.25	12.65	18.05	6.94	14.90	21.96	20.05	Y
4499.1925–4507.2181	15.6427	15.3519	0.0074	9	4.57	4.75	20.88	22.59	6.03	12.00	29.07	8.03	Y
4520.1843–4523.1715	15.5355	15.3618	0.0047	10	3.79	4.11	14.37	16.87	5.31	10.00	17.36	2.99	Y
4604.5218–4523.1715	15.7810	15.3618	0.0065	19	8.65	8.98	74.83	80.67	3.13	4.69	41.91	81.35	Y
4604.5218–4653.4045	15.7810	15.5159	0.0074	50	3.08	2.84	9.48	8.11	1.95	2.45	26.49	48.88	Y
4840.2995–4818.4134	15.8563	15.5457	0.0076	39	2.98	3.22	9.50	10.50	2.12	2.73	31.04	21.89	Y
4856.2391–4876.2416	15.8481	15.5259	0.0066	32	3.32	3.18	10.85	9.57	1.83	2.24	32.21	20.00	Y
4992.5052–4984.5065	15.7368	15.5003	0.0030	8	9.88	9.86	97.69	97.20	6.94	14.90	23.65	8.00	Y
5059.5278–5040.3400	15.8014	15.5101	0.0086	26	3.11	3.14	9.69	9.85	2.60	3.62	29.10	19.19	Y
5207.2032–5191.2163	15.7837	15.5506	0.0071	16	2.82	2.73	7.97	7.43	3.51	5.51	23.29	15.99	Y
5405.5290–5388.4588	15.5608	15.3273	0.0072	30	3.77	3.57	14.20	12.78	2.32	3.10	23.33	17.07	Y
5473.3549–5480.4003	15.6800	15.2445	0.0086	12	6.84	6.95	22.04	21.47	4.43	7.70	43.54	7.04	Y
5552.2920–5480.4003	15.6255	15.2445	0.0071	152	3.94	4.07	15.53	16.55	1.47	1.66	38.09	71.89	Y
6655.2381–6670.2057	15.6248	15.3574	0.0071	18	4.53	4.50	20.54	20.24	3.23	4.90	26.72	14.97	Y
6848.4617–6693.2131	15.5542	15.3491	0.0059	21	3.50	3.02	12.26	9.13	2.94	4.29	20.49	155.25	Y

Notes. Column (1): Observing time (JD). Column (2): Magnitude at the variability occurrence point (m_1). Column (3): Magnitude at the variability ending point (m_2). Column (4): Uncertainty of the corresponding night (σ). Column (5): Pairs of observations (N). Column (6): Variability index (C_1) from the difference in magnitude between target and comparison star ($O - S_1$). Column (7): Variability index (C_2) from the difference in magnitude between target and comparison star ($O - S_2$). Column (8): F-test value (F_1) from target and comparison star ($O - S_1$). Column (9): F-test value (F_2) from target and comparison star ($O - S_2$). Column (10): Critical value for the corresponding N at 99% level. Column (11): Critical value for the corresponding N at 99.9% level. Column (12): Variability amplitude (A%). Column (13): Corresponding timescale in units of days. Column (14): Variability (Y: has a variation).

A brightness variation of $\Delta R = 15.624 - 15.357 = 0.267$ mag, over a time interval of 14.98 days, was detected as shown in Figure 4(d).

3.2. Period Analysis

Periodicity analysis is interesting in blazars. However, it is not easy to investigate periods because of unevenly sampled observations. Here, we will perform the Jurkevich, discrete correlation function (DCF), and power spectrum analysis (PSA) methods using the *R*-band light curve.

Jurkevich: The Jurkevich method is based on the expected mean square deviation (Jurkevich 1971). All data are divided into *M* groups according to the stages around each bin, and the overall V_m^2 of each bin is calculated. A "good" test period has inconspicuous variation and an almost constant value compared to a "weak" test period. The uncertainty of the period is estimated by calculating the half-height full width corresponding to the valley value V_m^2 (Kidger et al. 1992).

DCF: The DCF method (Edelson & Krolik 1988; Hufnagel & Bregman 1992) studies the correlation between two series. If we performed it using only one time series, it could be adopted for period analysis (Fan & Lin 2000). To implement this method, we first calculated the unbinned correlation (UDCF) of two data sets (*a* and *b*), i.e.,

$$\mathrm{UDCF}_{ij} = \frac{(a_i - \langle a\rangle) \times (b_j - \langle b\rangle)}{\sqrt{\sigma_a^2 \times \sigma_b^2}}, \tag{5}$$

where a_i and b_j refer to two time series, $\langle a\rangle$ and $\langle b\rangle$ are the mean of the two data sets, and σ_a and σ_b are the corresponding standard deviations. Second, UDCF_{ij} with the same delay was averaged to obtain the DCF (τ) in the suitable size bin for each time interval. Its relationship was as follows:

$$\mathrm{DCF}(\tau) = \frac{1}{M}\sum \mathrm{UDCF}_{ij}(\tau), \tag{6}$$

where *M* is the total number of pairs. The standard deviation for each bin was

$$\sigma(\tau) = \frac{1}{M}\left(\sum[\mathrm{UDCF}_{ij} - \mathrm{DCF}(\tau)]^2\right)^{0.5}. \tag{7}$$

PSA: Since optical observation data are usually nonuniformly sampled time series, the Lomb–Scargle method (Lomb 1976; Scargle 1982) can be applied to this characteristic time series to estimate the major periodic components, but this algorithm seriously underestimates the eigenfrequency amplitude problem. In 1981, Ferraz-Mello (1981) proposed a date-compensated discrete Fourier transform (DCDFT), which uses the idea of function space projection to realize a Fourier transform and better solve the amplitude problem. When the data is nonuniformly sampled, for a single test frequency, the power and amplitude of the DCDFT can be defined as

$$P(\omega, |x) = \frac{N[\langle y|y\rangle - \langle 1|y\rangle^2]}{2S^2},$$
$$A(\omega, |x) = \sqrt{2[\langle y|y\rangle - \langle 1|y\rangle^2]}, \tag{8}$$

where *N* represents the number of data points, *y* represents the time simulation function, and S^2 represents the variance of the time series.

Although the DCDFT can better solve the existent problem of amplitude, when the DCDFT processes data with large and irregular time intervals, a large amount of aliasing will be generated. The complex CLEANest process can extract statistically significant and real periods from a complex power spectrum containing a large number of false peaks (Foster 1995). Additionally, false-alarm probability (FAP) is adopted for confidence analysis of the acquired signal. Please refer to the literature for the specific principle and calculation process of FAP (Horne & Baliunas 1986).

When Jurkevich was adopted for the *R*-band light curve, as can be seen from Figure 5, the Jurkevich curve was distributed with a "valley" of different depths. In the Jurkevich method, each "valley" represents a possible periodic component. Seven components were also detected by DCDFT+CLEANest. These seven "valleys" are marked by red dots on the Jurkevich curve, as shown in Figure 5. They are a period of $P_{\mathrm{J1}} = 2.72 \pm 0.52$ yr, a period of $P_{\mathrm{J2}} = 1.62 \pm 0.21$ yr, a period of $P_{\mathrm{J3}} = 1.31 \pm 0.07$ yr, a period of $P_{\mathrm{J4}} = 1.05 \pm 0.07$ yr, a period of $P_{\mathrm{J5}} = 0.92 \pm 0.17$ yr, a period of $P_{\mathrm{J6}} = 0.70 \pm 0.12$ yr, and a period of $P_{\mathrm{J7}} = 0.48 \pm 0.15$ yr. The seven components are listed in Column (1) in Table 5. In addition, Kidger et al. (1992) suggested that if the fraction reduction of a variance $f = \frac{1 - V_m^2}{V_m^2} > 0.5$ ($V_m^2 < 0.67$) for the component, then this component has a high confidence. The period and corresponding parameter (*f*) of each component are listed in Column (2) and Column (3) in Table 5.

For nonuniformly sampled time series, the DCDFT+CLEANest method has the best performance. Therefore, it can be used as our main measure for period analysis. We adopted it for the *R*-band light curves of our observations. We obtained the following DCDFT+CLEANest method analysis results, marking them with "P_{D}": $P_{\mathrm{D1}} = 2.72 \pm 0.41$ yr; the half-amplitude is 0.22, covering 19.3 yr. $P_{\mathrm{D2}} = 1.62 \pm 0.14$ yr and the half-amplitude is 0.20. $P_{\mathrm{D3}} = 1.31 \pm 0.10$ yr and the half-amplitude is 0.17. $P_{\mathrm{D4}} = 1.06 \pm 0.06$ yr and the half-amplitude is 0.13. $P_{\mathrm{D5}} = 0.92 \pm 0.05$ yr and the half-amplitude is 0.14. $P_{\mathrm{D6}} = 0.73 \pm 0.03$ yr and the half-amplitude is 0.15. $P_{\mathrm{D7}} = 0.48 \pm 0.01$ yr and the half-amplitude is 0.12. The parameters of the seven CLEANest components are listed in Column (5) and Column (7) of Table 5. In addition, we calculated the signal-to-noise ratio (S/N) of each CLEANest component using the software PERIOD04 (Lenz 2004; Yang et al. 2012; Li et al. 2016), and we list the calculation results in Table 5, Column (6). The period analysis results using DCDFT+CLEANest for the *R*-band data are shown in Figure 6. Using the red-noise autoregressive integral model, the 1 – FAP of all seven components is over 95% (red dashed curve), and that of four of them is over 99% (blue dashed curve). The results are listed in Table 5, Column (8).

Finally, for further testing, the results of optical *R*-band data processing with the DCF in this study are shown in Figure 7 (black solid curve). Plotting the simulated curve (blue solid curve) of the seven CLEANest components, we found that the simulated DCF curve matches the observed DCF curve well.

3.3. Physical Properties of Jets

In this section, we aim to investigate the jet physical properties of the source for the purpose of connecting jet properties and variability activity. A data set combined with our *R*-band data and archival multiwavelength data from the Space Science Data Centre (SSDC) for this source was compiled to fit a broadband SED. We employed the SED model proposed by Massaro et al. (2004, 2006) with a log-

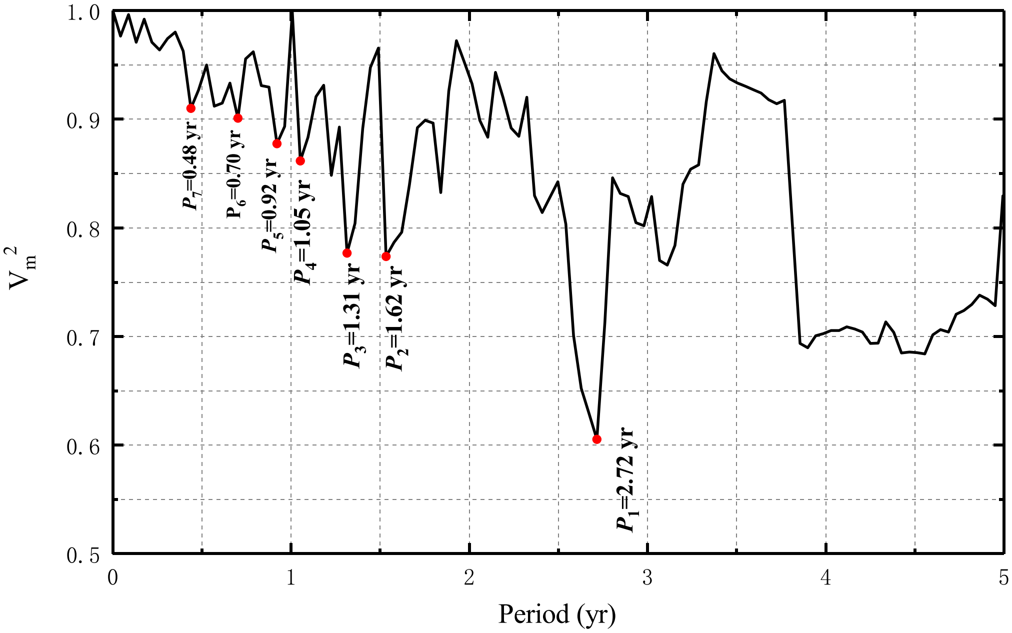

Figure 5. Jurkevich method result of 1ES 2344 + 514 in the optical *R*-band light curve. Red dots indicate components that were detected in DCDFT+CLEANest.

Table 5
Comparison of Results of DCDFT, Jurkevich, and CLEANest Periodic Analysis of the Light Curve

Jurkevich Time: 19.3 yr	$P_{\rm J}$ (yr)	f	PSA	$P_{\rm D}$ (yr)	S/N	A_R	1 − FAP (95%, 99%)
(1)	(2)	(3)	(4)	(5)	(6)	(7)	(8)
$P_{\rm J1}$	2.71 ± 0.52	0.65	$P_{\rm D1}$	2.72 ± 0.41	6.08	0.22	>, >
$P_{\rm J2}$	1.62 ± 0.21	0.29	$P_{\rm D2}$	1.62 ± 0.14	5.41	0.20	>, >
$P_{\rm J3}$	1.31 ± 0.23	0.28	$P_{\rm D3}$	1.31 ± 0.10	4.40	0.17	>, >
$P_{\rm J4}$	1.05 ± 0.07	0.16	$P_{\rm D4}$	1.06 ± 0.06	3.60	0.13	>, >
$P_{\rm J5}$	0.92 ± 0.17	0.13	$P_{\rm D5}$	0.92 ± 0.05	3.83	0.14	>, =
$P_{\rm J6}$	0.70 ± 0.12	0.11	$P_{\rm D6}$	0.73 ± 0.03	3.96	0.15	>, =
$P_{\rm J7}$	0.48 ± 0.15	0.09	$P_{\rm D7}$	0.48 ± 0.01	3.25	0.12	>, =

parabolic power law (LPPL) function of electron energy distribution coupled with the synchrotron and IC radiation mechanism in the framework of the one-zone model (Ghisellini et al. 1996; Tavecchio et al. 1998). An LPPL, where a particle energy distribution of a power-law function at the lower-energy tail becomes a log-parabola function at its higher-energy range (Tramacere et al. 2009, 2011), is expressed as follows:

$$N(\gamma) = \begin{cases} N_e(\gamma/\gamma_0)^{-s}\ , \gamma \leqslant \gamma_0, \\ N_e(\gamma/\gamma_0)^{-(s+r\cdot\log(\gamma/\gamma_0))}\ , \gamma > \gamma_0, \end{cases} \tag{9}$$

where N_e is the number density of electrons, γ_0 is the pivot energy of the electron spectrum, s is the spectral index, and r is the spectral curvature. In this SED model, we have six parameters, including the maximum energy of electrons ($\gamma_{\rm max}$) and the minimum energy of electrons ($\gamma_{\rm min}$), to describe the relativistic electron population in the dissipation region. Besides these, there are three other parameters—magnetic field (B), dissipation region size ($R_{\rm diss}$), and Doppler beaming factor (δ).

In addition, during the procedure of SED fitting at the VHE band, one must take into account the absorption of extragalactic background light (EBL). High-energy γ-ray photons are significantly absorbed by EBL photons, and the absorption could make the observed spectrum much steeper than the original spectrum at the VHE band for TeV BL Lac objects (Aharonian et al. 2006; Franceschini et al. 2008; Finke et al. 2010; Domínguez et al. 2011). We applied the EBL average model from Franceschini et al. (2008) to correct the attenuation at the VHE band (>100 GeV):

$$F_{\rm in}(\nu) = F_{\rm ob}(\nu)e^{-\tau(\nu,z)}, \tag{10}$$

where $\tau(\nu,\ z)$ is the optical depth, which is a function of frequency and redshift, as calculated by Franceschini et al. (2008).

In the present work, we introduce the Jets SED Modeler and Fitting Tool (JetSet)[10] (Tramacere et al. 2009, 2011) to generate the SED for 1ES 2344 + 514 and calculate the nine parameters (N_e, γ_0, $\gamma_{\rm min}$, $\gamma_{\rm max}$, s, r, B, $R_{\rm diss}$, and δ). JetSet is an open-source program for building the radiative and accelerative processes in relativistic jets, to fit numerical models to observed data. JetSet is able to find the optimal values of parameters through a Bayesian parameter estimation method based on Markov Chain Monte Carlo sampling.

We introduce the "average state" of blazar jets: the average state characterizes the general physical properties of jets in all

[10] https://jetset.readthedocs.io/en/latest/index.html

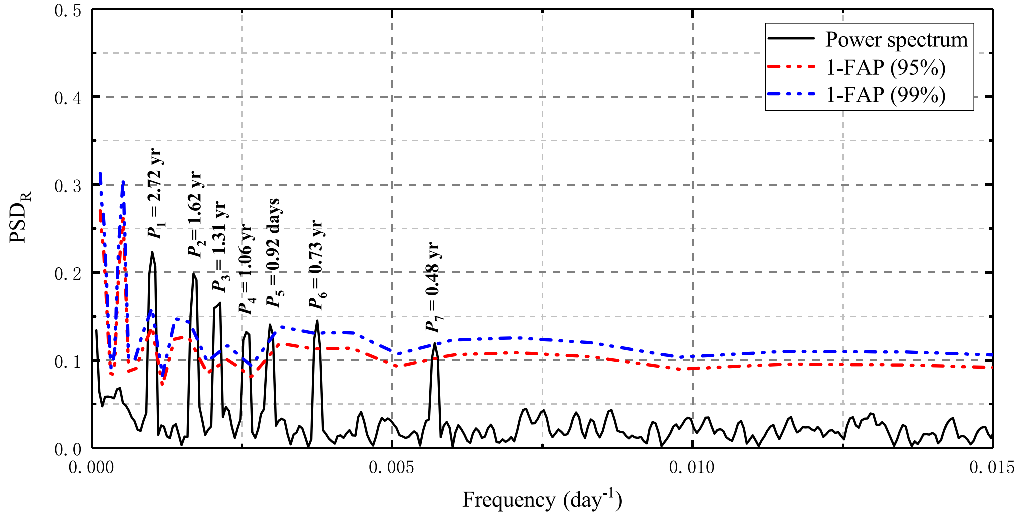

Figure 6. Periodic diagrams of 1ES 2344 + 514 in the optical *R*-band light curve as found by DCDFT+CLEANest. The black solid curve represents the Fourier power spectrum. The red and blue dashed curves represent the FAP levels of 95% and 99%, respectively.

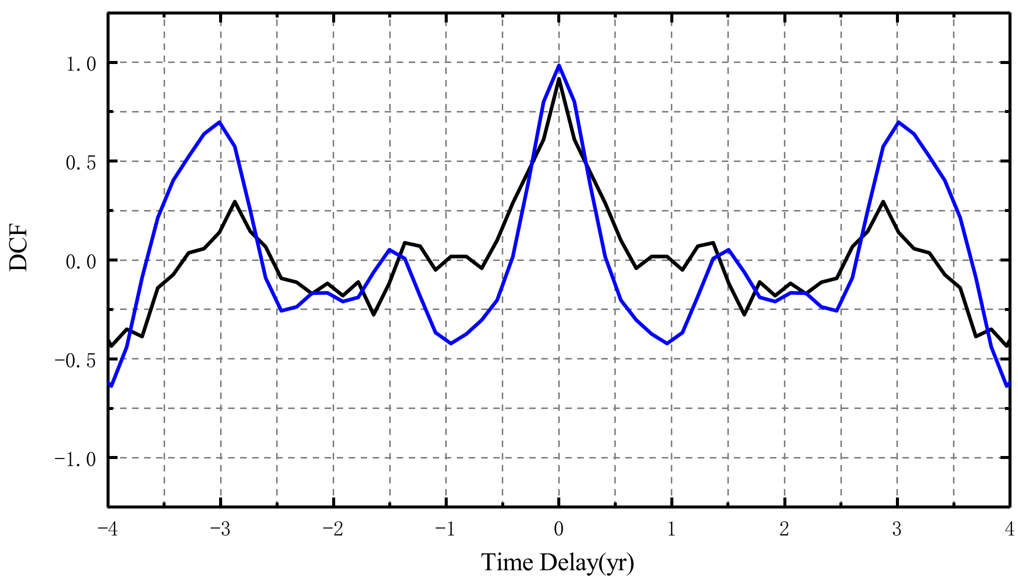

Figure 7. Periodic analysis of 1ES 2344 + 514 in the optical *R*-band light curve (black solid curve) was performed using the DCF. The DCFs of the theoretical light curves (blue solid curve) of the seven CLEANest components are given as a comparison.

observation campaigns. In order to model the average-state SED for our source, we prepared multiwavelength data from the SSDC after removing the flare events, which have been reported in literature (Catanese et al. 1998; Acciari et al. 2011), and modeled it through JetSet. Figure 8 shows our SED fitting result for the average state, and the parameters are listed in Table 6, including the nine parameters that describe the electron distribution and dissipation region. We note that the SED modeling result $\delta = 15.00$, which is close to the results of $\delta = 12.77$ (Ghisellini et al. 2014), $\delta = 19.46$ (Liodakis et al. 2018), $\delta = 16.06$ (Chen 2018), and $\delta = 12.54$ (Zhang et al. 2020). It shows that our modeling is reasonable.

The average-state model results provide us with a reference to further study activity in different states. 1ES 2344 + 514 was observed to have a remarkable VHE γ-ray flare (48% Crab Nebula flux) by the Very Energetic Radiation Imaging Telescope Array System (VERITAS) from 2007 December 7 to 2007 December 8. Simultaneous observation was performed by Swift Observatory in both the UV (with the Ultraviolet and Optical Telescope) and X-ray (with the X-Ray Telescope) bands (Burrows et al. 2005; Poole et al. 2008; Acciari et al. 2011). A broadband SED was modeled with a one-zone leptonic model. Taking advantage of the long-term monitoring, we also collected data during the remarkable-flare period. We added our *R*-band data, from 2007 October to 2008 January, into the contemporaneous data of this flare and revisited the "flare-state" SED with our model through JetSet. Before modeling the flare-state SED, we had to remove the host galaxy contribution from our *R*-band data (see Figure 9) at the *R* band. The flare-state SED fitting result, which is listed in Table 6, suggests that the flare was caused by strong radiation from a much larger dissipation region, even with a lower electron energy density and slightly larger Doppler factor, compared to that of the average state. In a comparison with Acciari et al. (2011), our model for the flare suggests a much larger dissipation region, a higher electron density, and a smaller

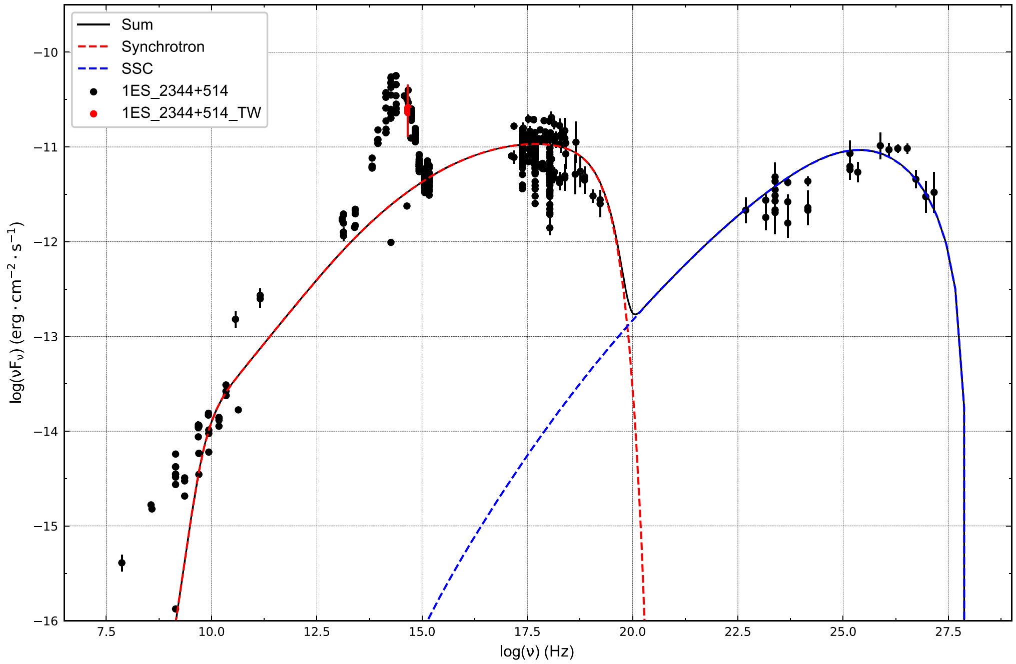

Figure 8. The SED fitting of 1ES 2344 + 514. The solid black line represents the EBL-corrected SED, the dashed red line represents the synchrotron radiation spectrum, and the dashed blue curve represents the IC emission curve from a synchrotron self-Compton (SSC) mechanism. The data set is twofold: SSDC-documented data (with flare data removed) are marked as black dots, and our *R*-band data are shown in red.

Table 6
The Parameters of the SED Modeling for 1ES 2344 + 514

Parameter	Average	Flare	Unit
N_e	5.00	2.30	cm^{-3}
γ_0	3.50×10^3	3.30×10^3	⋯
$\gamma_{\rm min}$	1.00×10^2	1.30×10^2	⋯
$\gamma_{\rm max}$	5.00×10^6	3.00×10^6	⋯
s	1.90	1.80	⋯
r	0.22	0.17	⋯
B	1.10×10^{-2}	1.20×10^{-2}	G
$R_{\rm diss}$	4.20×10^{16}	8.40×10^{16}	cm
δ	15.00	15.00	⋯
$\log\nu_{\rm Sy}$	17.68	18.02	Hz
$\log\nu_{\rm IC}$	25.43	25.96	Hz
$\log F_{\rm Sy}$	−10.94	−10.38	erg cm^{-2} s^{-1}
$\log F_{\rm IC}$	−11.03	−10.30	erg cm^{-2} s^{-1}

Doppler factor. There are two reasons for the difference in the two model results: (1) we have applied different electron energy distributions, an LPPL for our model and a broken power law for their model; (2) our *R*-band observation data was also considered in the flare SED fitting of our work.

According to our SED modeling result of the flare event, we suggest that there was a strong inner shock in the core, and the shock propagation changed the entire dissipation region environment. The shock strongly activated the plasma in the jet, and many more electrons were accelerated to being extremely relativistic, so that a much larger size of dissipation region was formed. Usually, this kind of flare event should contain superluminal motions of "knots" (Abeysekara et al. 2018; Nesci et al. 2021). However, there was no high-resolution radio observation during the 1ES 2344 + 514 flare period. The nearest Very Long Baseline Array (VLBA) observation in 2008 August, performed by the Monitoring of Jets in Active Galactic Nuclei with VLBA Experiments (MOJAVE) program (Lister et al. 2021), suggests a proper-motion speed of 0.03*c* when the flare event had faded far away.

4. Discussion and Conclusions

Variability is one of the typical observational properties of blazars. As a TeV blazar, 1ES 2344 + 514 has been studied in the optical bands in the past 20 years (Miller et al. 1999; Dai et al. 2001; Kurtanidze & Nikolashvili 2002; Xie et al. 2002; Kurtanidze et al. 2003; Fan et al. 2004; Kurtanidze et al. 2004, 2005; Ma et al. 2010; Gaur et al. 2012; Pandey et al. 2020). However, intraday variability has seldom been reported.

In this paper, optical *R*-band data of 1ES 2344 + 514 observed with a 70 cm meniscus telescope from 1998 to 2017 is presented and analyzed. We investigated the brightness variation characteristics on intraday, short-term variation, and long-term timescales. We examined the light curves of 628 nights using three statistical methods and found the largest variation during our monitoring period is $\Delta R = 1.154$ mag; we also found some STVs with timescales of 2.99–214.19 days. As for IDVs, we only detected one on one night during the whole monitoring period. IDVs are really rare for 1ES 2344 + 514. It is well known that as a point source, a strong host galaxy contribution will dilute (mask) the true variability. In the present work, when the host galaxy contribution with $R = 14.90$ mag (Nilsson et al. 1999) was removed, we found an IDV at JD 2,457,367 with a timescale of $\Delta T = 12.99$ minutes. Therefore, we propose that the host galaxy contribution is one of the factors that caused the rare IDV from 1ES 2344 + 514.

4.1. Magnetic Field Strength

As for the explanation of blazar multiwavelength variation, many models have been proposed, such as relativistic jet propagation in shocks (e.g., Marscher & Gear 1985; Hughes et al. 1991; Qian et al. 1991; Marscher et al. 1992; Wagner & Witzel 1995; Marscher 1996). In this model, there is a high

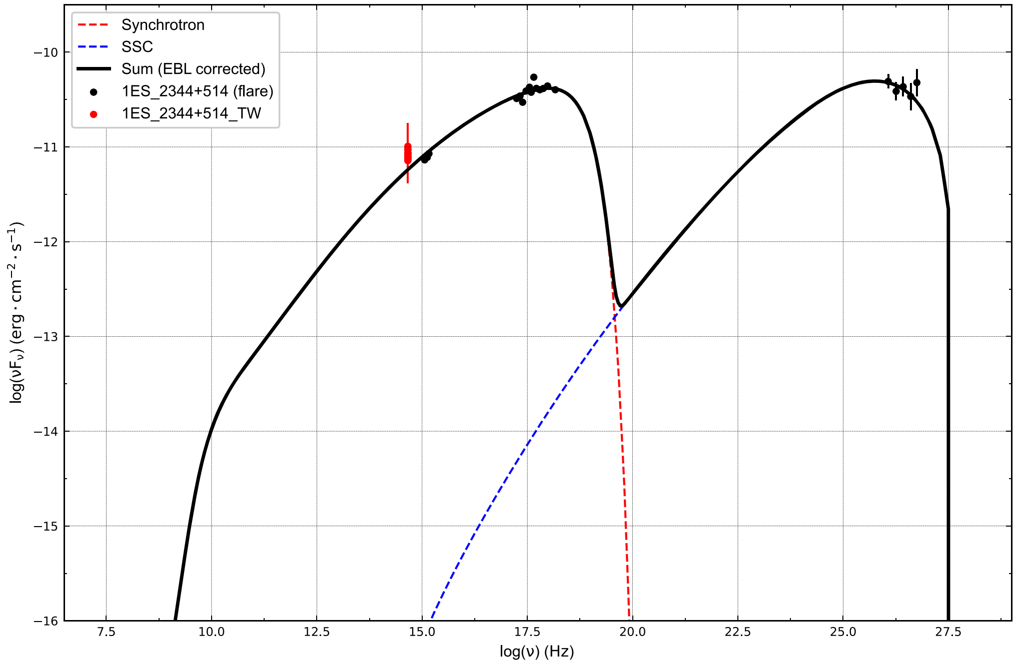

Figure 9. The SED fitting of a flare with quasi-simultaneous observation of 1ES 2344 + 514.

probability of rapid variation when a shock occurs in a relativistic jet. The spiral structure, precession, or geometric effects in the jet may also lead to rapid variation (e.g., Camenzind & Krockenberger 1992; Gopal-Krishna 1992). These models are general, though common, in terms of explaining variability timescales of days and months. In this section, a two-fluid model proposed by Sol et al. (1989) is used to explain the causes of rapid variation. These authors believed that the observed jet radiation is composed of two different fluids. The first fluid is a nonrelativistic jet of electron–proton plasma. It is responsible for carrying most of the mass and kinetic energy from the blazar central engine to outside of the galaxy. The second fluid consists of an electron–positron plasma. It forms a relativistic beam that enters the jet channel. Its particle number density is 10^{-1}–10^{-3} orders of magnitude lower than that of the first fluid. It is the source of superluminal velocities, with which this fluid is explained in detail in Henri & Pelletier (1991). The observed characteristics of some sources also support the two-fluid model (e.g., 3C 120 and 0917+624). Under reasonable assumptions, the Kelvin–Helmholtz instability will occur at the junction of two jet components with different velocities and electron number densities. As a result, the beam produces significant disturbances. However, a stronger magnetic field prevents or delays the development of instability, such as density inhomogeneity and jet column bending (Romero 1995). Romero (1995) suggested that if the magnetic field intensity exceeds a critical value, it inhibits the development of such instability:

$$B_c = [4\pi N_e M_e c^2(\Gamma^2 - 1)]^{1/2}\Gamma^{-1}, \tag{11}$$

where N_e represents the electron number density, M_e the electron rest mass, and Γ the bulk Lorentz factor. If the magnetic field is stronger than a given critical value B_c, instability is suppressed. Conversely, if the magnetic field intensity is lower than the critical value B_c, the Kelvin–Helmholtz instability will develop, resulting in significant changes in the morphological characteristics of the beam, which may be responsible for the rapid changes in relativistic shock-wave interaction. According to Equation (11), we can know that with the increase of electron number density, the incidence of IDVs in the light curve will increase.

In our SED modeling, we obtained an electron number density $N_e = 5.00$ cm^{-3} and a Doppler factor $\delta = 15.00$. If the viewing angle of the blazar is small, sin $(\theta) \approx 1/\Gamma$, then $\delta \approx \Gamma$ (Ghisellini et al. 2014), and Equation (11) can be expressed as

$$B_c \approx [4\pi N_e M_e c^2(\delta^2 - 1)]^{1/2}\delta^{-1}, \tag{12}$$

so we obtain a critical magnetic field intensity value $B_c = 2.37 \times 10^{-3}$ G. We find that the critical magnetic field intensity B_c is less than the result $B = 1.10 \times 10^{-2}$ G given by our SED fitting, that is, the strong magnetic field does not destroy the jet's morphological characteristics. Although we found one IDV in 628 nights, the incidence of IDVs can be considered rather low. Therefore, we think that a high magnetic field intensity is probably one of the factors that prevent IDV. In addition, 1ES 2344 + 514 is a high-energy-peaked blazar (HBL) source; therefore our results also support the conclusion in Gaur et al. (2012) that low-energy-peaked blazars are more prone to IDV behavior than HBLs.

4.2. Quasiperiodic Oscillation Analysis

It is common for a light curve to show periodic variation in AGNs. It is proposed that the reason for the year-scale periodicity is a binary black hole in the central region. OJ 287, NGC 3597, PKS 1510-089, 3C 273, and 3C 454.3 have been considered by researchers as candidates for binary black hole sources (Sillanpaa et al. 1988; Forbes & Hau 2000; Romero et al. 2000; Xie et al. 2002; Fan et al. 2021). In our work, 1ES 2344 + 514 is another candidate for the binary black hole source. Thus, we investigated this by going into a year-scale period analysis of 1ES 2344 + 514.

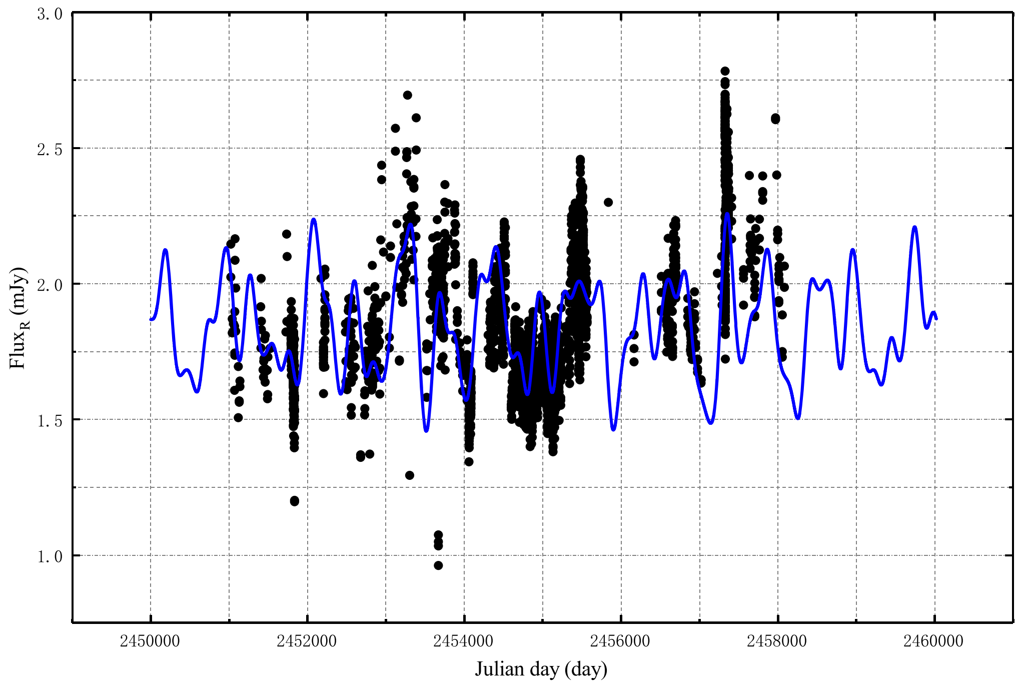

Figure 10. The theoretical light curve (blue solid curve) and the observed light curve (black filled dots) are presented.

In our work, we used three different period analysis methods (Jurkevich, DCDFT+CLEANest, and DCF) to analyze the light curve of 1ES 2344 + 514. The DCF method was used to verify the consistency of seven CLEANest components with observed light curves—Fan et al. (2021) did a similar DCF analysis for 3C 454.3. We averaged the Jurkevich and DCDFT +CLEANest method results to obtain the following: $\langle P_1\rangle = 2.72 \pm 0.47$ yr, $\langle P_2\rangle = 1.61 \pm 0.18$ yr, $\langle P_3\rangle = 1.31 \pm 0.17$ yr, $\langle P_4\rangle = 1.05 \pm 0.07$ yr, $\langle P_5\rangle = 0.92 \pm 0.11$ yr, $\langle P_6\rangle = 0.70 \pm 0.08$ yr, and $\langle P_7\rangle = 0.48 \pm 0.08$ yr. We show the theoretical light curve obtained by using the seven CLEANest periods in Figure 10. Hence, we think that there are four long-term periods (2.72, 1.61, 1.31, and 1.05 yr).

We also found quasiperiodic oscillations (QPOs) ranging from $\langle P_5\rangle = 0.92 \pm 0.11$ yr to $\langle P_7\rangle = 0.48 \pm 0.08$ yr. The variability mechanism is perhaps similar to that of the about 2 months of QPO in 3C 66A in Lainela et al. (1999), that of the 47 days of QPO found in 3C 454.3 by Sarkar et al. (2021), and that of the 34.5 days of QPO in γ-ray emission from PKS 2247-131 (Zhou et al. 2018). This timescale QPO can be explained by the spiral structure in the jet. Judging from the timescale QPOs, it is possible that binary supermassive black holes exist in 1ES 2344 + 514.

The highest S/N and the highest half-amplitude result are for $P_1 = 2.72$ yr (S/N = 6.08, $A_R = 0.22$) in the R-band analysis results. Therefore, we detected $P = 2.72$ yr as the observational period ($P_{\rm ob}$) in the R-band light curve.

For a binary black hole system, according to Kepler's third law, one can derive the following relation:

$$P_{\rm int}^2 = \frac{4\pi^2(a+b)^3}{G(M+m)}, \tag{13}$$

where $P_{\rm int}$ is the intrinsic orbital period ($P_{\rm int} = P_{\rm ob}/(1+z)$), $a + b$ is the sum of the semimajor and semiminor axes, G is the gravitational constant, and M and m are the masses of the primary and secondary black holes (Fan et al. 2014, 2021);

$$P_{\rm int} \sim 1.72 M_8^{-1/2} r_{16}^{3/2}\left(1 + \frac{m}{M}\right)^{-1/2} \text{yr}, \tag{14}$$

where M_8 is the mass of the main black hole in units of $10^8 M_\odot$, the orbital radius $r_{16} = a + b$, and the unit of this radius is 10^{16} cm. For 1ES 2344 + 514, we used $M = 80.80 M_8$ (Woo & Urry 2002) as the mass of the primary black hole. If the second black hole has the same mass as the primary black hole (i.e., $m/M \sim 1$; Qian et al. 2007), then we adopt a period value $P_{\rm int} = 2.61$ yr. We can obtain a sum of semiaxes $r = 7.18 \times 10^{16}$ cm.

Binary black hole systems can be used as gravitational wave candidates. When the orbit of a binary black hole system becomes smaller with the evolution of gravitational radiation, its lifetime is estimated as (Romero et al. 2003)

$$\tau_{\rm merge} = \frac{5}{256}\frac{c^5}{G^3}\frac{r^4}{(m+M)^2}\frac{1}{\mu}, \tag{15}$$

where $\mu = \frac{mM}{m+M}$ represents the reduced mass. Then, we can calculate the lifetime of the binary black hole as $\tau_{\rm merge} = 6.24 \times 10^2$ yr. Begelman et al. (1980) suggested that if a binary black hole system becomes sufficiently tight, the orbital shrinking timescale of the gravitational radiation

$$\tau_{\rm EG} \sim 3.0 \times 10^5 \left(\frac{m}{M}\right)^{-1} M_8^{-3} r_{16}^4 \text{ yr}, \tag{16}$$

and therefore, for 1ES 2344 + 514, we have $\tau_{\rm EG} = 1.51 \times 10^3$ yr. Because $\log(\tau_{\rm merge}) = 2.80$ is close to $\log(\tau_{\rm EG}) = 3.17$, the binary black hole system is very closely connected.

4.3. Conclusion

In this work, we present our observations from the TeV BL Lac object 1ES 2344 + 514 carried out with the 70 cm telescope at Abastumani Observatory, Georgia, from 1998 to 2017, and analyze its variability on different timescales. Three periodic analysis methods are adopted for the optical R-band light curve and a binary black hole system is used to explain the long-term period. We can come to the following conclusions:

1. An intraday variability of $\Delta R = 0.155$ mag (15.356 – 15.201 mag) over a timescale of $\Delta T = 12.99$ minutes is detected once during our 628 days of monitoring.
2. According to the Kelvin–Helmholtz thermal instability, we propose that the reason IDVs have seldom been detected from 1ES $2234+514$ is that the magnetic field is higher than the critical value B_c, which reduces the incidence of IDVs in the light curves.
3. The physical parameters of the dissipation region are obtained by fitting the SED with a one-zone SSC model. We obtain the theoretical results for both the average state and flare state, and we think the flare may be caused by plasma activation during shock propagation.
4. Periods of $P = 2.72 \pm 0.47$, 1.61 ± 0.18, 1.31 ± 0.17, and 1.05 ± 0.07 yr are obtained from the R-band light curve. The orbital parameters of the binary black hole system are obtained, if we take 2.72 yr as the orbital period. The sum of the semiaxes is $r = 7.18 \times 10^{16}$ cm. We also obtain the lifetime of the binary black hole: $\tau_{\rm merge} = 6.24 \times 10^{2}$ yr.

Thanks are given to the reviewer for the constructive comments and suggestions. The work is partially supported by the National Natural Science Foundation of China (NSFC U2031201 and NSFC 11733001) and the Natural Science Foundation of Guangdong Province (2019B030302001). We also acknowledge science research grants from the China Manned Space Project with No. CMS-CSST-2021-A06, and support from Astrophysics Key Subjects of Guangdong Province and Guangzhou City. S.O.K. acknowledges financial support from the Shota Rustaveli National Science Foundation under contract PHDF-18-354.

ORCID iDs

J. T. Cai https://orcid.org/0000-0002-8960-1544
O. M. Kurtanidze https://orcid.org/0000-0001-5385-0576
J. H. Fan https://orcid.org/0000-0002-5929-0968

References

Abdo, A. A., Ackermann, M., Agudo, I., et al. 2010, ApJ, 716, 30
Abdollahi, S., Acero, F., Ackermann, M., et al. 2020, ApJS, 247, 33
Abeysekara, A. U., Benbow, W., Bird, R., et al. 2018, ApJ, 856, 95
Acciari, V. A., Aliu, E., Arlen, T., et al. 2011, ApJ, 738, 169
Ackermann, M., Ajello, M., Atwood, W. B., et al. 2015, ApJ, 810, 14
Aharonian, F., Akhperjanian, A. G., Bazer-Bachi, A. R., et al. 2006, Natur, 440, 1018
Aharonian, F. A. 2000, NewA, 5, 377
Aharonian, F. A. 2002, MNRAS, 332, 215
Angel, J. R. P., & Stockman, H. S. 1980, ARA&A, 18, 321
Begelman, M. C., Blandford, R. D., & Rees, M. J. 1980, Natur, 287, 307
Blandford, R. D., & Koenigl, A. 1979, ApL, 20, 15
Blandford, R. D., & Rees, M. J. 1978, in Pittsburgh Conf. on BL Lac Objects, ed. A. M. Wolfe (Pittsburgh, PA: Univ. of Pittsburgh), 328
Błażejowski, M., Sikora, M., Moderski, R., & Madejski, G. M. 2000, ApJ, 545, 107
Bloom, S. D., & Marscher, A. P. 1996, ApJ, 461, 657
Burrows, D. N., Hill, J. E., Nousek, J. A., et al. 2005, SSRv, 120, 165
Camenzind, M., & Krockenberger, M. 1992, A&A, 255, 59
Catanese, M., Akerlof, C. W., Badran, H. M., et al. 1998, ApJ, 501, 616
Cellone, S. A., Romero, G. E., & Combi, J. A. 2000, AJ, 119, 1534
Chen, L. 2018, ApJS, 235, 39
Ciaramella, A., Bongardo, C., Aller, H. D., et al. 2004, A&A, 419, 485
Ciprini, S., Takalo, L. O., Tosti, G., et al. 2007, A&A, 467, 465
Dai, B. Z., Xie, G. Z., Li, K. H., et al. 2001, AJ, 122, 2901
de Diego, J. A. 2010, AJ, 139, 1269
Dermer, C. D., & Schlickeiser, R. 1993, ApJ, 416, 458
Domínguez, A., Primack, J. R., Rosario, D. J., et al. 2011, MNRAS, 410, 2556
Edelson, R. A., & Krolik, J. H. 1988, ApJ, 333, 646
Fan, J.-H. 2005, ChJAS, 5, 213
Fan, J.-H., Bastieri, D., Yang, J.-H., et al. 2014, RAA, 14, 1135
Fan, J.-H., Kurtanidze, O. M., Nikolashvili, M. G., et al. 2004, ChJAA, 4, 133
Fan, J. H., & Lin, R. G. 2000, ApJ, 537, 101
Fan, J. H., Lin, R. G., Xie, G. Z., et al. 2002, A&A, 381, 1
Fan, J. H., Peng, Q. S., Tao, J., Qian, B. C., & Shen, Z. Q. 2009a, AJ, 138, 1428
Fan, J. H., Xie, G. Z., Pecontal, E., Pecontal, A., & Copin, Y. 1998, ApJ, 507, 173
Fan, J. H., Zhang, Y. W., Qian, B. C., et al. 2009b, ApJS, 181, 466
Fan, J. H., Liu, Y., Yuan, Y. H., et al. 2007, A&A, 462, 547
Fan, J. H., Yang, J. H., Liu, Y., et al. 2016, ApJS, 226, 20
Fan, J. H., Kurtanidze, O., Liu, Y., et al. 2017a, ApJ, 837, 45
Fan, J. H., Yang, J. H., Xiao, H. B., et al. 2017b, ApJL, 835, L38
Fan, J. H., Tao, J., Liu, Y., et al. 2018, AJ, 155, 90
Fan, J. H., Kurtanidze, S. O., Liu, Y., et al. 2021, ApJS, 253, 10
Fan, Z., Cao, X., & Gu, M. 2006, ApJ, 646, 8
Ferraz-Mello, S. 1981, AJ, 86, 619
Finke, J. D., Razzaque, S., & Dermer, C. D. 2010, ApJ, 712, 238
Forbes, D. A., & Hau, G. K. T. 2000, MNRAS, 312, 703
Foster, G. 1995, AJ, 109, 1889
Franceschini, A., Rodighiero, G., & Vaccari, M. 2008, A&A, 487, 837
Gaur, H., Gupta, A. C., & Wiita, P. J. 2012, AJ, 143, 23
Ghisellini, G., Maraschi, L., & Dondi, L. 1996, A&AS, 120, 503
Ghisellini, G., Tavecchio, F., Maraschi, L., Celotti, A., & Sbarrato, T. 2014, Natur, 515, 376
Giommi, P., Padovani, P., & Perlman, E. 2000, MNRAS, 317, 743
Gopal-Krishna, & Wiita, P. J. 1992, A&A, 259, 109
Grube, J. 2008, in AIP Conf. Proc. 1085, High-energy Gamma-Ray Astronomy, ed. F. A. Aharonian, W. Hofmann, & F. Rieger (Melville, NY: AIP), 585
Gupta, A. C. 2014, JApA, 35, 307
Hartman, R. C., Villata, M., Balonek, T. J., et al. 2001, ApJ, 558, 583
Heidt, J., & Wagner, S. J. 1996, A&A, 305, 42
Henri, G., & Pelletier, G. 1991, ApJL, 383, L7
Horne, J. H., & Baliunas, S. L. 1986, ApJ, 302, 757
Hufnagel, B. R., & Bregman, J. N. 1992, ApJ, 386, 473
Hughes, P. A., Aller, H. D., & Aller, M. F. 1991, ApJ, 374, 57
Jurkevich, I. 1971, Ap&SS, 13, 154
Kidger, M., Takalo, L., & Sillanpaa, A. 1992, A&A, 264, 32
Kurtanidze, O. M., & Nikolashvili, M. G. 2001a, in IAU Symp. 205, Galaxies and their Constituents at the Highest Angular Resolutions, ed. R. T. Schilizzi (Cambridge: Cambridge Univ. Press), 80
Kurtanidze, O. M., Nikolashvili, M. G., Ritz, S., Gehrels, N., & Shrader, C. R. 2001b, in AIP Conf. Proc. 587, Gamma 2001: Gamma-Ray Astrophysics, ed. S. Ritz, N. Gehrels, & C. R. Shrader (Melville, NY: AIP), 333
Kurtanidze, O. M., & Nikolashvili, M. G. 2002, Blazar Astrophysics with BeppoSAX and Other Observatories, ed. P. Giommi, E. Massaro, & G. Palumbo (Frascati: ESA-ESRIN), 189
Kurtanidze, O. M., Nikolashvili, M. G., Kapanadze, B. Z., et al. 2004, NuPhS, 132, 193
Kurtanidze, O. M., Nikolashvili, M. G., Kimeridze, G. N., et al. 2005, MmSAI, 76, 53
Kurtanidze, O. M., Richter, G. M., & Nikolashvili, M. G. 1999, Blazar Monitoring towards the Third Millennium, Proc. of the OJ-94 Annual Meeting 1999, ed. C. M. Raiteri, M. Villata, & L. O. Takalo (Pino Torinese: Osservatorio Astronomico di Torino), 29
Kurtanidze, O. M., Sikharulidze, M. A., Nikolashvili, M. G., Kapanadze, B., & Urushadze, T. 2003, A&AT, 22, 699
Lainela, M., Takalo, L. O., Sillanpää, A., et al. 1999, ApJ, 521, 561
Lenz, P. 2004, CoAst, 144, 41
Li, H.-L., Wei, J.-Y., Yang, Y.-G., & Dai, H.-F. 2016, RAA, 16, 2
Li, H. Z., Chen, L. E., Yi, T. F., et al. 2015, PASP, 127, 1
Liodakis, I., Hovatta, T., Huppenkothen, D., et al. 2018, ApJ, 866, 137
Lister, M. L., Homan, D. C., Kellermann, K. I., et al. 2021, ApJ, 923, 30
Liu, F. K., Liu, B. F., & Xie, G. Z. 1996, A&AS, 123, 569
Lomb, N. R. 1976, Ap&SS, 39, 447

Ma, L., Xie, G. Z., Yi, T. F., et al. 2010, Ap&SS, 327, 35
Maraschi, L., Ghisellini, G., & Celotti, A. 1992, ApJL, 397, L5
Marscher, A. P. 1996, in ASP Conf. Ser. 110, Blazar Continuum Variability, ed. H. R. Miller, J. R. Webb, & J. C. Noble (San Francisco, CA: ASP), 248
Marscher, A. P., & Gear, W. K. 1985, ApJ, 298, 114
Marscher, A. P., Gear, W. K., & Travis, J. P. 1992, in Variability of Blazars, ed. E. Valtaoja & M. Valtonen (Cambridge: Cambridge Univ. Press), 85
Massaro, E., Perri, M., Giommi, P., & Nesci, R. 2004, A&A, 413, 489
Massaro, E., Tramacere, A., Perri, M., Giommi, P., & Tosti, G. 2006, A&A, 448, 861
Mead, A. R. G., Ballard, K. R., Brand, P. W. J. L., et al. 1990, A&AS, 83, 183
Meyer, F., & Meyer-Hofmeister, E. 1984, A&A, 132, 143
Miller, H. R., Carini, M. T., & Goodrich, B. D. 1989, Natur, 337, 627
Miller, H. R., Daya, A. B., & Ferrara, E. C. 1999, in ASP Conf. Ser. 159, BL Lac Phenomenon, ed. L. O. Takalo & A. Sillanpää (San Francisco, CA: ASP), 75
Nesci, R., Cutini, S., Stanghellini, C., et al. 2021, MNRAS, 502, 6177
Nieppola, E., Tornikoski, M., & Valtaoja, E. 2006, A&A, 445, 441
Nilsson, K., Pasanen, M., Takalo, L. O., et al. 2007, A&A, 475, 199
Nilsson, K., Pursimo, T., Takalo, L. O., et al. 1999, PASP, 111, 1223
Nolan, P. L., Abdo, A. A., Ackermann, M., et al. 2012, ApJS, 199, 31
Padovani, P., & Giommi, P. 1996, MNRAS, 279, 526
Pandey, A., Gupta, A. C., Damljanovic, G., et al. 2020, MNRAS, 496, 1430
Perlman, E. S., Stocke, J. T., Schachter, J. F., et al. 1996, ApJS, 104, 251
Poole, T. S., Breeveld, A. A., Page, M. J., et al. 2008, MNRAS, 383, 627
Qian, B., & Tao, J. 2004, PASP, 116, 161
Qian, S. J., Quirrenbach, A., Witzel, A., et al. 1991, A&A, 241, 15
Qian, S.-J., Kudryavtseva, N. A., Britzen, S., et al. 2007, ChJAA, 7, 364
Raiteri, C. M., Ostorero, L., Massaro, E., et al. 2012, A&A, 402, 151
Rani, B., Gupta, A. C., Joshi, U. C., Ganesh, S., & Wiita, P. J. 2010, ApJL, 719, L153
Rieger, F. M. 2004, ApJL, 615, L5
Romero, G. E. 1995, Ap&SS, 234, 49
Romero, G. E., Cellone, S. A., & Combi, J. A. 1999, A&AS, 135, 477
Romero, G. E., Cellone, S. A., & Combi, J. A. 2000, A&A, 360, L47
Romero, G. E., Fan, J.-H., & Nuza, S. E. 2003, ChJAA, 3, 513
Sagar, R., Gopal-Krishna, & Wiita, P. J. 1996, MNRAS, 281, 1267
Sarkar, A., Gupta, A. C., Chitnis, V. R., & Wiita, P. J. 2021, MNRAS, 501, 50
Scargle, J. D. 1982, ApJ, 263, 835
Scarpa, R., & Falomo, R. 1997, A&A, 325, 109
Schlafly, E. F., & Finkbeiner, D. P. 2011, ApJ, 737, 103
Sikora, M., Begelman, M. C., & Rees, M. J. 1994, ApJ, 421, 153
Sillanpaa, A., Haarala, S., Valtonen, M. J., Sundelius, B., & Byrd, G. G. 1988, ApJ, 325, 628
Sol, H., Pelletier, G., & Asseo, E. 1989, MNRAS, 237, 411
Stetson, P. B. 1987, PASP, 99, 191
Tavecchio, F., Maraschi, L., & Ghisellini, G. 1998, ApJ, 509, 608
Tramacere, A., Giommi, P., Perri, M., Verrecchia, F., & Tosti, G. 2009, A&A, 501, 879
Tramacere, A., Massaro, E., & Taylor, A. M. 2011, ApJ, 739, 66
Urry, C. M., & Padovani, P. 1995, PASP, 107, 803
Valtonen, M., Kidger, M., Lehto, H., & Poyner, G. 2008, A&A, 477, 407
Veron-Cetty, M. P., & Veron, P. 1993, A Catalogue of Quasars and Active Nuclei, ESO Scientific Report, (Garching: European Southern Observatory)
Wagner, S. J., & Witzel, A. 1995, ARA&A, 33, 163
Wiita, P. J. 2011, JApA, 32, 147
Woo, J.-H., & Urry, C. M. 2002, ApJL, 581, L5
Wu, J., Zhou, X., Peng, B., et al. 2005, MNRAS, 361, 155
Xiao, H., Fan, J., Yang, J., et al. 2019, SCPMA, 62, 129811
Xie, G. Z., Zhou, S. B., Dai, B. Z., et al. 2002, MNRAS, 329, 689
Xie, G. Z., Zhou, S. B., Li, K. H., et al. 2004, MNRAS, 348, 831
Xiong, D., Bai, J., Zhang, H., et al. 2017, ApJS, 229, 21
Yang, Y. G., Li, H. L., & Dai, H. F. 2012, AJ, 143, 13
Zhang, L., Chen, S., Xiao, H., Cai, J., & Fan, J. 2020, ApJ, 897, 10
Zhang, X., Xie, G., & Bai, J. 1998, AcApS, 18, 260
Zhou, J., Wang, Z., Chen, L., et al. 2018, NatCo, 9, 4599